Huesa Carmen (Orcid ID: 0000-0002-4989-4258)
McInnes Iain B. (Orcid ID: 0000-0003-4449-8501)
Goodyear Carl S (Orcid ID: 0000-0001-5926-5941)

The IκB protein BCL3 controls osteogenesis and bone health

Hussain Jaffery[1] (PhD), Carmen Huesa[1,4] (PhD), Sabarinadh Chilaka[1] (PhD), John Cole[1] (MRes), James Doonan[1] (PhD), Moeed Akbar[1] (PhD), Lynette Dunning[4], Kathleen Elizabeth Tanner[2,3] (PhD, FRSEng, FRSE, OBE), Rob J van 't Hof[5] (PhD), Iain B McInnes[1] (PhD, MB ChB, CBE), Ruaidhrí J Carmody[1] (PhD), Carl S Goodyear[1]* (PhD)

[1]School of Infection & Immunity, University of Glasgow, Glasgow, G12 8QQ, United Kingdom

[2]James Watt School of Engineering, University of Glasgow, Glasgow, G12 8QQ, United Kingdom

[3]Current address: School of Engineering and Materials Science and Institute of Bioengineering, Queen Mary University of London, London, E1 4NS, United Kingdom

[4]Institute of Biomedical & Environmental Health, University of the West of Scotland, Paisley, PA1 2BE, United Kingdom

[5]Institute of Ageing and Chronic Disease, University of Liverpool, Liverpool, L69 3BX, United Kingdom

*Correspondence to: Professor Carl S Goodyear, School of Infection & Immunity, University of Glasgow, Glasgow, G12 8QQ, UK; Carl.Goodyear@glasgow.ac.uk

This article has been accepted for publication and undergone full peer review but has not been through the copyediting, typesetting, pagination and proofreading process which may lead to differences between this version and the Version of Record. Please cite this article as doi: 10.1002/art.42639

Acknowledgements

Funding for this work was generously provided by the Wellcome Trust as part of a PhD studentship (099786/Z/12/Z and 099786/Z/12/A) and by the Research into Inflammatory Arthritis Centre Versus Arthritis (RACE) (22072). Funding for research collaboration was also provided by the Bone Research Society Travel Fellowship.

Contributions

CSG, RJC and HJ conceived the study and designed the experiments. HJ, CH, SC, JC, JD, LD, and MA performed experiments and produced data. KET, RJVH, IBM provided analytical and experimental resources. HJ and CSG wrote the manuscript. All authors reviewed the manuscript.

Competing Interests

The authors declare no competing interests.

Abstract

Objective

IκB protein B-cell lymphoma 3-encoded protein (BCL3) is a regulator of the NF-κB family of transcription factors. NF-κB signalling fundamentally influences the fate of bone-forming osteoblasts and bone-resorbing osteoclasts, but the role of BCL3 in bone biology has not been investigated. The objective of this study was to evaluate BCL3 in skeletal development, maintenance and osteoarthritic pathology.

Methods

To assess the contribution of BCL3 to skeletal homeostasis, neonatal mice (n = 6-14) lacking BCL3 (*Bcl3*$^{-/-}$) and WT controls were characterised for bone phenotype and density. To reveal the contribution to bone phenotype by the osteoblast compartment in *Bcl3*$^{-/-}$ mice, transcriptomic analysis of early osteogenic differentiation and cellular function (n = 3-7) were assessed. Osteoclast differentiation and function in *Bcl3*$^{-/-}$ mice (n = 3-5) was assessed. Adult 20-week *Bcl3*$^{-/-}$ and WT mice bone phenotype, strength and turnover were assessed. A destabilisation of the medial meniscus (DMM) model of osteoarthritic ostephytogenesis was utilised to understand adult bone formation in *Bcl3*$^{-/-}$ mice (n = 11-13).

Results

Evaluation of *Bcl3*$^{-/-}$ mice revealed congenitally increased bone density, long bone dwarfism, increased bone biomechanical strength and altered bone turnover. Molecular and cellular characterisation of mesenchymal precursors showed that

Bcl3$^{-/-}$ cells display an accelerated osteogenic transcriptional profile that leads to enhanced differentiation into osteoblasts with increased functional activity; which could be reversed with a mimetic peptide. In a model of osteoarthritis-induced osteophytogenesis, *Bcl3*$^{-/-}$ mice exhibit decreased pathological osteophyte formation ($P < 0.05$).

Conclusion

Cumulatively, these findings demonstrate that BCL3 controls developmental mineralisation to enable appropriate bone formation, whilst in a pathological setting it contributes to skeletal pathology.

Introduction

Homeostatic bone growth and subsequent skeletal maintenance is a tightly controlled process that relies on the coordination of osteoblasts (depositing mineralised matrix) and osteoclasts (resorbing matrix) (1). The differentiation, interaction and ensuing function of these cells are regulated by both extracellular factors (i.e., metabolites, bone morphogenetic proteins (BMPs), fibroblast growth factors (FGFs), Wnt family proteins, macrophage colony stimulating factor (M-CSF), receptor activator of nuclear factor-kappa-light-chain-enhancer of activated B cells (NF-κB) ligand (RANKL) (2,3), and intracellular factors including NF-κB (4). Perturbation of this closely regulated system can contribute to decreased bone quality and pathology observed in diseases such as osteoarthritis, rheumatoid arthritis and osteoporosis.

The NF-κB family of transcription factors is critical in determining the differentiation and activities of cells affecting skeletal development and maintenance. Combined, this family functions as a master regulator of gene transcription. Members are characterised by the presence of the Rel homology domain (RHD), which mediates dimerization and DNA binding (5). NF-κB activation involves a cascade of events, including receptor ligation, activation of IκB kinases (IKKs) and phosphorylation and degradation of IκBs, which ultimately triggers the nuclear translocation of NF-κB dimers (5). The generation of homo- or hetero-dimers is based on the interaction of five subunits (p65/RelA, RelB, c-Rel, p50/NF-κB1 and p52/NF-κB2) that can bind to specific DNA sequences (κB sites) in the target promoters of hundreds of genes (6). Notably, homodimers of the p50 and p52 NF-κB subunits, which lack trans-activation domains (TADs), interact with the atypical IκB protein B-cell lymphoma 3 (BCL3) (5). BCL3, initially identified as a proto-oncogene,

is a predominantly nuclear protein containing seven ankyrin repeat domains (ANKRD) (5). Upon tumour necrosis factor (TNF) receptor (TNFR) or toll-like receptor (TLR)-driven NF-κB activation, BCL3 stabilises p50 homodimers at NF-κB binding sites (κB sites), preventing p50 degradation and competitively inhibiting transactivating p65 or c-Rel containing NF-κB dimers from occupying the κB sites (5). Moreover, it has been speculated that the interaction of BCL3 with homodimers of p50 and p52 leads to recruitment of additional transcriptional co-repressors or co-activators (5). The physiological role of Bcl3 is well-described as a regulator of adaptive immunity through control of T and B cell maturation and formation of lymph node germinal centres (7).

Prior studies have investigated the role of NF-κB in osteoblast and osteoclast differentiation and function. In osteoblasts, NF-κB activation has been reported to both induce and inhibit osteogenesis. For instance, TNF-driven NF-κB activation can reduce bone formation by inhibiting RUNX2, an osteoblast-lineage specific transcription factor, which subsequently disrupts BMP signalling (8). Activity of the IKK complex has been implicated in inhibiting osteoblast activity (9). Furthermore, disruption of NIK results in increased p100 levels, leading to increased bone formation and osteoblast numbers, whilst disruption of RelB increases bone formation (10,11). In juxtaposition, activation of NF-κB can enhance early osteogenesis and p65/RelA is essential for osteoblast activity and survival (12,13). Finally, low-dose TNF can increase osteogenesis via NF-κB activation (14). Taken together, this illustrates that the role of NF-κB activity in regulating osteoblast differentiation is complex and context-specific.

In osteoclast differentiation, the binding of RANKL to RANK, leads to NF-κB activation (4). Notably, the RANK gene *Tnfrsf11a* possesses κB sites at the proximal

promoter region, which facilitate a feed-forward RANKL response (15). Furthermore, RelB/p65 dimers strongly induce the central osteoclastogenic transcription factor NFATc1, thereby increasing osteoclast differentiation, survival and function (4). Mice lacking the NF-κB p50 and p52 subunits exhibit severe dwarfism, a thickened hypertrophic chondrocyte layer, severe osteopetrosis and an absence of osteoclasts (16).

Although it is accepted that NF-κB plays an essential role in bone biology, the specific contribution of BCL3 in shaping bone is ill-defined. Herein, we show that BCL3-deficient (*Bcl3*$^{-/-}$) neonatal mice have congenitally increased bone mineral density and truncated long bones, compared to WT counterparts. The observed increased bone matrix in *Bcl3*$^{-/-}$ mice is explained by an acceleration of the osteogenic transcriptional program. This increase in bone density is maintaned into maturation (20-week old mice); however, at this stage, although there is increased bone density and associated biomechanical strength, new bone formation is inhibited. Finally, in a model of pathological osteophytogenesis, we demonstrate that *Bcl3*$^{-/-}$ mice have reduced ectopic osteophyte formation. Collectively, our data illustrate that BCL3 is an intrinsic regulator of osteoblast and osteoclast differentiation and thus a modulator of skeletal health.

Materials and Methods

Detailed information for the following materials methods, and methods for quantitative PCR, osteoclast differentiation and functional assessment are described in the Supplementary Methods.

Animals.

Bcl3$^{-/-}$ and WT littermates were bred under standard conditions (17,18). All animal studies received ethical approval from the University of Glasgow and were performed under a UK Home Office licence.

Micro-CT analysis of neonates.

Post-natal day 0, mice were scanned via micro-CT (4.5μm resolution). Reconstructions were manually analysed using DataViewer (version 1.5.2.4) Visualisations were rendered in CTvox (version 3.1.1).

Calvarial osteoblast isolation and differentiation.

Calvaria were dissected from neonatal mice (post-natal days 3 to 5) and digested in collagenase II solution (Gibco). Cells were expanded for 3 days, subsequently seeded at 1.25x10^4 cells/well and cultured for an additional 3 days. Osteogenic Medium (supplemented with 50μg/ml ascorbic acid and 2mM β-glycerophosphate)

was added to initiate osteogenesis (day 0). In certain cultures, 30μM BCL3 mimetic peptide (BDP2) or mutated peptide (mBDP2) was added.

RNAseq library preparation and sequencing.

Cells were lysed using 700μL of QIAzol Lysis Reagent (QIAGEN). RNA purification was performed as per standard manufacturer instructions using the miRNeasy Mini Kit (QIAGEN). cDNA synthesis was carried out using the SMART-seq v4 Ultra Low Input RNA Kit for Sequencing (Clontech). Library preparation was conducted using the Low Input Library Prep Kit HT (Clontech), as per instructions. Sequencing was conducted using the Illumina HiSeq 4000 System with a read-depth of ~36million/sample, of 75bp paired-end reads.

Bioinformatic analysis.

Differential expression between the four groups was calculated using DESeq2. Final expression values were represented as fragments per kilobase of exon per million reads (FPKMs). Statistical cutoff of adjusted $P < 0.05$ was considered significant. Downstream analysis utilised the PANTHER gene ontology (GO) enrichment analysis tool (19). Transcription factor binding site (TFBS) analysis was conducted of the region 350bp upstream and 50bp downstream of the gene transcription start site, using HOMER (20). Protein-protein functional association network clustering analysis involved MCL clustering with a 1.2 inflation parameter (21). The RNA sequencing data are deposited in NCBI's Gene Expression Omnibus and are accessible through GEO Series accession number GSE125153 (https://www.ncbi.nlm.nih.gov/geo/query/acc.cgi?acc=GSE125153).

Histological assessment of osteoblast cultures.

Alkaline phosphatase assay and Alizarin Red staining was conducted as previously described(22). Sircol staining was performed on fixed cells using Sircol Sirius Red (Biocolor) soluble dye solution. Image analysis was conducted via Fiji/ImageJ (version 2.0) packages and involved thresholding of dark pixels (23).

Micro-CT analysis of adult long bones.

Micro-CT images of whole fixed deskinned adult legs were acquired on the SkyScan 1272 micro-CT scanner (Bruker). Images were processed by a back-projection method using NRecon (version 1.6.10.4). Specialised macros for the trabecular and cortical regions in the CT Analyser (version 1.16.4.1) software enabled quantitative analysis on the various volumes.

Biomechanical analyses.

Tibiae were assessed in 3-point flexure (bend) tests using a 50N load cell affixed to a calibrated 3-point apparatus (Zwick Roell) with a 10mm/min force advancement, and data recorded until fracture. Femurs were placed in a 2kN load cell (Zwick Roell) with a displacement rate of 0.1mm/s and data was recorded until fracture occurred.

Dynamic histomorphometry and histology.

Mice were intraperitoneally injected with 15 mg/kg calcein dye (Sigma-Aldrich) solution in DPBS on day -5 and -2, prior to harvest. Femurs were fixed, embedded in methyl methacrylate (MMA) resin, and cut into 5μm sections. For dynamic histomorphometry, slides were counter-stained with a 1% Calcein Blue (Sigma-Aldrich) and fluorescent intra-label thickness was quantified. For histological

assessment of the growth plate, slides were dual-stained with Safranin O and Fast Green.

Bone turnover ELISAs.

Enzyme immunoassays were used to detect serum levels of P1NP and CTX1 (Immunodiagnostic Systems) and OPG and RANKL (R&D Systems), according to manufacturer's instructions.

Experimental osteoarthritis model.

Destabilisation of the medial meniscus (DMM) (on 10-week old male) and subsequent micro-CT analysis was performed as previously described (24).

Statistical approach.

For statistical analysis, GraphPad Prism (versions 7-9) and R packages were utilised. *P*-values and adjusted *P*-values less than 0.05 were considered significant.

Results

BCL3 alters skeletal development.

To investigate whether congenital skeletal abnormalities are associated with loss of BCL3, neonatal (postnatal day 0) wild type (WT) and *Bcl3*$^{-/-}$ mice were examined by X-ray micro-computed tomography (micro-CT; Figure 1a). Gross skeletal abnormalities were absent in *Bcl3*$^{-/-}$ pups; however, analysis of the complete skeleton revealed that *Bcl3*$^{-/-}$ neonatal mice had an increase in overall bone mineral density, relative to WT (Figure 1b). This was also associated with a significant reduction in the length of mineralised long bones (including the humerus, ulna, radius, tibia and femur) in *Bcl3*$^{-/-}$ mice, compared to WT controls (Figure 1c).

Further interrogation of glycan-rich cartilage (Alcian Blue staining) and calcium mineral (Alizarin Red staining) in whole-mount skeletons, uncovered altered skeletal composition in *Bcl3*$^{-/-}$ neonatal mice. Notably, *Bcl3*$^{-/-}$ neonates had demonstrably increased Alizarin Red staining in their long bones (e.g. tibia), compared to WT controls, indicative of increased bone mineral density and osteoblast hyperactivity (Figure 1d). This was further supported by specific quantitative analysis of Alizarin Red staining in the tibial diaphysis (Figure 1e). Histological analysis (Safranin O and Fast Green staining) revealed a decrease in the cartilaginous growth plate height of 4-week *Bcl3*$^{-/-}$ mice, compared to WT controls; indicative of perturbation of the osteochondro lineage, (Figure 1f). Combined, these data suggest that loss of BCL3 results in over-active mineralisation, coupled to reduced overall long bone growth.

Bcl3$^{-/-}$ osteoblast transcriptome shows an accelerated early osteogenesis signature.

To determine whether the increased bone density observed in *Bcl3*$^{-/-}$ neonates was a result of altered osteoblast differentiation and activity, the temporal transcriptional profile of WT and *Bcl3*$^{-/-}$ cells during osteogenic differentiation was evaluated. Calvarial osteoblast precursors were isolated from WT and *Bcl3*$^{-/-}$ neonates and differentiated in the presence of L-ascorbic acid (AA) and β-glycerophosphate (BGP) for 1 or 3 days (Figure 2a). Principal component analysis (PCA) of all genes, across the two time-points in WT and *Bcl3*$^{-/-}$ samples, revealed that the bulk of variation (component 1) grouped the samples by genotype and time (Figure 2b). Hierarchical clustering of the significantly (false discovery rate-adjusted *P*-value < 0.05) up- and down-regulated transcripts (Figure 2c, Supplementary Figure 1 and Supplemental Data) confirmed this and revealed that, at both time points, *Bcl3*$^{-/-}$ osteoblasts maintained an altered transcriptome relative to WT cells. To understand whether this represented an enhanced progression of *Bcl3*$^{-/-}$ cells through the osteogenic process, further analysis was performed to fully evaluate the altered transcriptional profiles. Initially, a comparison of the temporal (day 1 vs day 3) difference (Δ) in fold-change (FC) of all expressed genes between WT and *Bcl3*$^{-/-}$ cells revealed that transcriptional programmes in both genotypes were highly correlated and shared a substantial proportion of significantly different genes (Supplementary Figures 1a and 1c). These data demonstrate that both WT and *Bcl3*$^{-/-}$ cells share a very similar transcriptional programme, namely osteogenesis.

The WT osteogenic programme (Δ WT) was better correlated with, and shared a larger proportion of, significant genes between WT and *Bcl3*$^{-/-}$ cells at day 1 (Δ Day 1) than at day 3 (Δ Day 3; Supplementary Figures 1b and 1d-e). Collation of all genes up- or downregulated between WT and *Bcl3*$^{-/-}$ cells into a relative metagene reinforced the progressive osteogenic phenomenon, and also highlighted

the day 1 upregulated metagene in *Bcl3*$^{-/-}$ cells (Supplementary Figure 1f). Comparison of the day 1 differentially *upregulated* genes in *Bcl3*$^{-/-}$ osteoblasts with the ΔWT signature differential genes at day 1 and day 3, revealed that *Bcl3*$^{-/-}$ day 1 cells were more similar to day 3 WT cells (228 overlapping transcripts) than day 1 WT cells (1 overlapping transcript; Supplementary Figure 1g). Notably, some of the genes consistently upregulated in *Bcl3*$^{-/-}$ cells versus WT at day 1 and WT at day 3 included *Apoe*, *Col3a1*, *Col14a1*, *Chrdl1*, *Bglap2*, *Bmp2*, *Fbn2*, *Mmp3*, *Mmp9*, *Postn*, *Sfrp1*, *Stat1*, *Tmem178*, *Steap4*, *Wnt16 and Igfbp3* (Supplementary Data). Taken together, this suggests that all cells are engaging in an osteogenic program, and already by day 1, *Bcl3*$^{-/-}$ cells are progressing through the process at an accelerated rate.

To further confirm the nature of the transcriptional program, gene ontology (GO) analyses for broad biological process and specific molecular function were performed for the genes upregulated in *Bcl3*$^{-/-}$ cells at day 1 (Supplementary Figures 1h-i). Notably, genes involved in extracellular matrix organisation and ossification were amongst the most-enriched processes (Supplementary Figure 1h). Molecular function analysis revealed an enrichment of genes that participate in extracellular matrix interaction and modification, with gene products involved in 'Wnt-protein binding' being the most enriched set (Supplementary Figure 1i). Classification of genes into the 'ossification' gene-set (most relevant to osteoblast function), and the most enriched 'Wnt-protein binding' gene-set clearly illustrated the enhanced level of expression in *Bcl3*$^{-/-}$ cells (Figure 2d). Functional clustering of the 281 genes *exclusively* upregulated in *Bcl3*$^{-/-}$ cells at day 1 compared to WT, revealed two gene subsets (Supplementary Figure 1j). GO 'biological process' / 'molecular function' analyses identified one cluster surrounding the TNF and IL-6

nodes with ‘immune response’ / ‘cytokine binding’ ontologies and another tight cluster with ‘cell cycle’ / ‘ATP binding’ ontologies. Transcription factor binding site analysis revealed upstream enrichment of known NF-κB p65 sites and enrichment sites most similar to p50 and p52 binding motifs, specific to the immune response gene cluster.

To validate the RNAseq findings, quantitative PCR was undertaken to evaluate osteoblast-specific matrix encoding genes including *Alpl*, *Col1a1* and *Ocn*. Notably, these transcripts were significantly increased at day 1 in *Bcl3*$^{-/-}$ osteoblasts, compared to WT controls (Figure 2e). Moreover, transcript levels of *Rankl* were higher and levels of *Opg* lower, in *Bcl3*$^{-/-}$ osteoblasts compared to WT (Figure 2e). Suggesting an altered osteoblast activity that could increase early crosstalk between osteoblasts and osteoclasts. The early-stage Wnt-driven prototypical osteoblast transcription factor, *Runx2*, also had elevated transcripts in *Bcl3*$^{-/-}$ osteoblasts compared to WT, while the later-stage Wnt-inhibiting transcription factor, osterix, had unchanged transcript levels (Figure 2e). Finally, expression of the ligand Wnt16 was confirmed to be elevated. Together, these data indicate that *Bcl3*$^{-/-}$ osteoblasts undergo an accelerated early osteogenesis programme.

BCL3 controls osteoblast differentiation.

To investigate the functional consequences of the accelerated osteogenesis transcriptional programme identified in *Bcl3*$^{-/-}$ pre-osteoblasts, *in vitro* differentiation assays were undertaken and cultures characterised for mature osteoblast-associated features. This included alkaline phosphatase (ALP), the prototypical osteoblast ectoenzyme that makes PO_4 available for mineralisation, which was markedly elevated in *Bcl3*$^{-/-}$ cultures compared to WT cultures at day 1 (Figure 3a)

(25). Moreover, production of collagen (for extracellular secretion and incorporation into bone; Figure 3b) and calcium mineralisation (microscopic bone nodules; Figure 3c) were also substantially increased in *Bcl3*$^{-/-}$ cultures, compared to WT controls. Full characterisation of calcified bone nodule formation to the point of osteoblast maturity (day 21) revealed a significantly increased cumulation of mineralised bone in *Bcl3*$^{-/-}$ cultures, compared to WT controls (Figure 3d). Combined with our transcriptome analysis these data demonstrate that lack of BCL3 enhances osteoblast differentiation and increased function.

We next investigated whether the accelerated osteoblast differentiation and increased osteogenic function in cells deficient in BCL3 could be reversed by treating *Bcl3*$^{-/-}$ cells with a BCL3 mimetic peptide (BDP2) (26). Analysis of cultures on day 3 showed a significant decrease in ALP expression in the BDP2-treated *Bcl3*$^{-/-}$ cultures compared to cells treated with an inactive control peptide (Figure 3e). Notably, similar results were obtained for BDP2-treated WT cells (Figure 3e). Thus, a mimetic BCL3 peptide substantially restricts osteogenic differentiation, placing BCL3 as a strong regulator of osteogenesis.

Osteoclastogenesis and resorption are controlled by BCL3.

To assess whether the increase in skeletal bone density observed in neonatal *Bcl3*$^{-/-}$ mice was due exclusively to increased osteoblast activity, or if perturbation of intrinsic osteoclast activity may be involved, osteoclastogenesis was assessed. Adult mouse bone marrow myeloid cells were differentiated *in vitro* using M-CSF and RANKL (Figure 4a). Evaluation of 6-day differentiated cultures demonstrated that loss of BCL3 results in a significant increase in the number and size of mature osteoclasts, compared to WT controls (Figure 4b). This also corresponded with an

increase in resorptive activity (Figure 4c) in *Bcl3*$^{-/-}$ osteoclasts relative to WT cells. Notably, the increased resorptive activity of *Bcl3*$^{-/-}$ osteoclasts was supressed by treatment with BDP2 peptide (Figure 4d).

To assess the impact of loss of BCL3 in the osteoblasts lineage and how this subsequently alters osteoclastogenesis, osteoblast-osteoclast co-cultures were conducted. Adult mouse WT CD14^{+} bone marrow-derived monocyte precursors were cultured with WT or *Bcl3*$^{-/-}$ long bone-derived mature osteoblasts for 9 days (Figure 4e). Assessment of osteoclastogenesis revealed that, compared to WT, co-culture with *Bcl3*$^{-/-}$ osteoblasts resulted in significant smaller and fewer less mature osteoclast (Figure 4f). Notably, this corresponded with significantly lower levels of RANKL but substantially higher levels of osteoprotegerin (OPG) in *Bcl3*$^{-/-}$ co-culture supernatants, relative to WT (Figure 4g). Moreover, the corresponding RANKL/OPG ratio was significantly increased for WT osteoblast co-cultures (Figure 4g). While *Bcl3*$^{-/-}$ osteoblasts did produce increased levels of *Wnt16* transcript and WNT16 protein compared to WT, levels in co-cultures were not significantly increased, thus excluding differential WNT16 involvement in coupling with osteoclasts (Supplementary Figure 2b-d). Evaluation of osteoclasts (cathepsin K^{+}) in 12-week adult tibiae revealed that there was a significant decrease in osteoclast number per tissue area in *Bcl3*$^{-/-}$ mice, compared to WT; whilst the number of osteoclasts per bone perimeter, was unchanged, explained by the increased bone in *Bcl3*$^{-/-}$ sections (Supplementary Figure 2e). Together, these data suggest that while BCL3 loss increases intrinsic osteoclastogenesis, it simultaneously enhances the ability of osteoblasts to restrict osteoclastogenesis, thus maintaining equilibrium.

Adult mice lacking BCL3 have denser, stronger bones.

Having identified increased skeletal mineral density in *Bcl3*$^{-/-}$ neonates and perturbation in both the osteoblast and osteoclast lineages, it was important to assess the impact on the adult skeleton. To achieve this, 20-week old WT and *Bcl3*$^{-/-}$ male mice (which represent the peak adult-stage of bone density, length and thickness) were analysed by micro-CT (27). Morphometric analysis focused on the medullary trabecular regions of the distal femur and the proximal tibia, and the distal cortical region of the femur (Figure 5a and Supplementary Figures 3-5). In both trabecular regions, percent bone volume density, trabecular number and trabecular thickness were increased in *Bcl3*$^{-/-}$ mice, compared to WT (Figure 5a and Supplementary Figures 3-4). Additionally, in *Bcl3*$^{-/-}$ mice, the bone surface to volume ratio and structural model index were significantly decreased in both trabecular regions; whereas, only the tibial region showed increased tissue volume and degree of anisotropy, compared to WT (Supplementary Figures 3 and 4b). In the femoral cortical region, *Bcl3*$^{-/-}$ mice displayed significantly increased mean total cross-sectional bone area, mean total cross-sectional tissue area and cross-sectional thickness, compared to WT (Supplementary Figure 5a). Furthermore, *Bcl3*$^{-/-}$ mice were also significantly different from WT in all other cortical morphometric parameters indicative of larger, more stable cortical bone (Supplementary Figure 5b).

To assess whether the increased bone density of *Bcl3*$^{-/-}$ male 20-week mice altered the biomechanical properties of load-bearing bones, a three-point break test of the tibial mid-diaphysis was conducted. Force-displacement curves for *Bcl3*$^{-/-}$ mice were significantly different from those of WT mice (Figure 5b), and were used to derive key biomechanical parameters. Essentially, *Bcl3*$^{-/-}$ tibiae had significantly increased ultimate load, stiffness and work to failure, when compared to WT;

indicative of increased biomechanical strength (Figure 5b). The femoral neck break test was also performed to support these findings and further demonstrated that *Bcl3*$^{-/-}$ bones have increased biomechanical strength, as defined by ultimate load and stiffness (Supplementary Figure 6).

To investigate new bone mineralisation in the adult (20-week old) skeleton, dynamic histomorphometry of femoral sections from mice administered with calcein double-label were assessed. Analysis of femurs showed that, by 20 weeks, *Bcl3*$^{-/-}$ mice had a decreased mineral apposition rate (MAR), when compared to WT controls (Figure 5c). To further explore bone turnover, serum markers P1NP (procollagen type 1 amino-terminal peptide; associated with bone formation) and CTX1 (carboxyl-terminal crosslinks peptide of type 1 collagen; associated with bone resorption) were evaluated. The levels of P1NP were significantly lower in the serum of *Bcl3*$^{-/-}$ mice compared to WT controls, whilst the levels of CTX1 were not significantly different from WT mice (Figure 5d). Serum levels of the osteoblast-osteoclast coupling factor RANKL were unchanged, but levels of its decoy competitor, OPG, were significantly increased in 20-week *Bcl3*$^{-/-}$ mice, compared to WT (Figure 5d); however, RANKL/OPG ratio was unchanged (P = 0.04, median of differences = 0.02, Wilcoxon test). Combined, this suggests that adult *Bcl3*$^{-/-}$ mice maintain increased bone density and strength, but the osteoblast-driven turnover/mineralisation rate of bone has decelerated by 20 weeks of age.

Absence of BCL3 restricts pathological osteophytic formation.

Given the accelerated osteogenesis in neonates, increased bone density in adults, mixed with a decrease in bone formation in *Bcl3*$^{-/-}$ mice, it was important to assess the *in vivo* mineralisation of new bone in adults. In order to achieve this, *Bcl3*$^{-/-}$ and

WT mice were subjected to destabilisation of the medial meniscus (DMM), which leads to the generation of new, ectopic mineralisation in the form of osteophytes (24). Fourteen days post-surgery, micro-CT analysis revealed that in the affected medial region of the tibial subchondral bone, protruding mineralised osteophyte projections were visibly reduced in *Bcl3*$^{-/-}$ mice, compared to WT controls (Figure 6a). Quantification of the total osteophyte bone volume showed that *Bcl3*$^{-/-}$ mice had significantly lower osteophyte bone volume, when compared to WT counterparts (Figure 6b). Histopathologcial scoring of articular cartilage at the medial tibial plateau showed that compared to WT, *Bcl3*$^{-/-}$ mice had a lower deterioration (Figures 6c and 6d). The histological evaluation also revealed that pathological articular cartilage fibrillation and cartilaginous osteophyte extension were present in WT, but reduced in *Bcl3*$^{-/-}$ mice (Figure 6d). Notably, unlike WT mice, *Bcl3*$^{-/-}$ mice did not have a significantly increased subchondral osteosclerosis in the bone loading regions of the tibial plateau of DMM-induced knees compared to contralateral controls, indicative of reduced disease (Figure 6e and Supplementary Figure 7).

Taken together, these data demonstrate that loss of BCL3 inhibits pathologically-driven new bone formation/mineralisation in adults, whilst maintaining increased congenic global bone density.

Discussion

The tightly regulated equilibrium between osteoblasts and osteoclasts determines skeletal development and maintenance. The master transcription factor, NF-κB, plays a key role in the differentiation of both cell types, and is thus crucial for maintaining skeletal health (4). In the present study, we have shown that BCL3, a

known regulator of NF-κB, has an integral role in modulating skeletal development and maintenance. Assessment of neonates clearly demonstrated that loss of BCL3 leads to an increase in bone density that was coupled with impeded long bone elongation. Transcriptomic analysis revealed that this was associated with an accelerated differentiation programme in *Bcl3*$^{-/-}$ osteoblast precursors that drove increased osteogenesis, which ultimately resulted in increased bone matrix production. Intrinsic osteoclastogenesis was shown to be regulated by BCL3, and ultimately restricted by osteoblast coupling through the RANKL-OPG axis. Surprisingly, although the increased bone density (and associated superior biomechanical strength) in *Bcl3*$^{-/-}$ mice was maintained into adulthood, osteoblast-driven generation of new bone was substantially decreased. This adult-specific phenotype was also associated with suppression of osteosclerosis and osteophytogenesis in the DMM model of osteoarthritic disease.

The altered bone biology observed in *Bcl3*$^{-/-}$ mice is reflective of the major role BCL3 plays in the regulation, rather than complete control, of NF-κB family members (5). This is illustrated by the more profound bone phenotypes seen in other NF-κB family member knockouts. For instance, double-deletion of p50 and p52, both of which interact with BCL3 (5), results in dwarfism and severe osteopetrosis (16). The "regulatory" nature of BCL3 is further supported by prior studies showing that (a) BCL3 is key for the maintenance of murine embryonic stem cell pluripotency and subsequent differentiation; with overexpression substantially attenuating but not blocking cell differentiation (28), and (b) over-expression of BCL3 in the myeloid lineage reducing, but not completely blocking, RANKL-driven osteoclastogenesis (29). Both observations are analogous to those seen in the *in vitro* osteoblastogenesis and osteoclastogenesis mimetic peptide cultures (Figures 3

and 4). Combined, and added to the observation that the transcriptional programme in the osteoblast lineage is accelerated (Figure 2), this supports the concept that BCL3 acts as a negative regulator of the critical NF-κB machinery involved in the differentiation programmes of multiple skeletal cell-types.

In the mesenchymal cell lineage, BCL3 has recently been shown to regulate crosstalk between Wnt signalling pathway components (30). Moreover, NF-κB p65 activation (driven by low-dose TNF), with subsequent signalling through the Wnt pathway, substantially increases osteogenic function (14). It is therefore noteworthy that the accelerated transcriptional response in *Bcl3*$^{-/-}$ pre-osteoblasts included enhancement of genes involved in Wnt regulation. In particular, increased expression of *Wnt16*, which provides a mechanism linking transient NF-κB activity to enhanced subsequent osteogenic activity (31-33). Interestingly, mutations in *Wnt16* were recently identified as some of the most significantly associated with risk of fracture, whilst Wnt16 was found to inhibit chondrocyte hypertrophy and be protective against osteoarthritis progression (34-36). We showed increased expression of both *Wnt16* transcript and protein in *Bcl3*$^{-/-}$ osteoblasts. Furthermore, the transcription factor signature of *Bcl3*$^{-/-}$ cells reveals a propensity for increased NF-κB p65, p50 and p52 transcriptional activation, alongside altered cell cycle and energetics-associated transcription factors. The transcription factors PU.1, IRFs, STATs, evidently involved in early osteogenesis in both WT and *Bcl3*$^{-/-}$ cells, are known to cooperate with each other especially in the immune cells wherein BCL3 is critical alongside NF-κB at gene promoters in a myriad of ways (37).

Increased osteogenic mineralisation in early development, followed by reduced osteoblast-driven bone turnover in *Bcl3*$^{-/-}$ mice is a model analogous to the

increased mineralisation occurring in WT male mice, versus females; wherein, females have a lower initial mineral apposition rate at 1 week of age, but exceed that of males by 20 weeks of age (27). Thus, increased density and strength concurrent with reduced bone formation (decreased P1NP and MAR) by 20 weeks is further evidence of accelerated skeletal maturation and an altered steady-state in adulthood. *Bcl3*$^{-/-}$ osteoblasts in co-culture regulate osteoclast differentiation by tipping the RANKL/OPG ratio in favour of reduced osteoclastogenesis, indicating an inhibition of bone resorption. The decreased bone formation along with the reduction of osteoclast differentiation depicts an adult bone with reduced bone remodeling in the absence of BCL3, which ultimately results in maintenance of developmental-driven bone mass.

The decrease in osteophytogenesis we observed in *Bcl3*$^{-/-}$ mice links to the tempered ability to generate new mineralised bone in adults. Osteophyte formation in the DMM model is associated with a characteristic chondrocytic core, which leads to progressive mineralisation; in a process reminiscent of endochondral ossification (24). We posit that in *Bcl3*$^{-/-}$ mice, the chondrocyte-osteoblast lineage favours osteoblastic differentiation, impeding endochondral bone elongation in neonates and leading to a reduced chondrocytic core and suppressing the formation of pathology-driven osteophytes in adults. Simultaneously, the osteophyte model functions to affirm the inverse relationship between increased bone density and endochondral protrusion (27,38). The subdued effect on subchondral bone change in DMM-induced *Bcl3*$^{-/-}$ mice is coupled with the reduction of osteophytogenesis as pathological indicators and likely involve the same osteochondro-lineage dynamics that are causal to the increased bone density in *Bcl3*$^{-/-}$ mice.

One of the limitations of our study was that we did not investigate osteochondro-progenitor differentiation into chondrocytes, or the process of chondrocyte-driven endochondral ossification (39-41). Chondrogenic differentiation, proliferation and hypertrophy is controlled by NF-κB subunit p65 activity (42,43). Nevertheless, recent work supports our model and provides evidence for role of BCL3 in chondrocytic callus-driven fracture healing, wherein *Bcl3*$^{-/-}$ mice exhibited delayed chondrocyte hypertrophy that was rescued with BCL3 overexpression (44). It is interesting to speculate therefore, given the inverse role of NF-κB during osteoblast and chondrocyte differentiation (4), that loss of BCL3 fundamentally pivots NF-κB such that differentiation of osteochondro-progenitors favours the osteoblast lineage. To fully interrogate this hypothesis additional studies using conditional *Bcl3*$^{-/-}$ mice are required.

In summary, our study definitively shows that BCL3 plays a major role in the control of osteoblast and osteoclast differentiation and crosstalk, which fundamentally regulates bone turnover and skeletal maintenance(Figure 6f). Beyond elucidating BCL3 function, this has implications for furthering understanding of NF-κB in the skeleton and for possible therapeutic targets in skeletal pathologies.

References:

1. Chen X, Wang Z, Duan N, Zhu G, Schwarz EM, Xie C. Osteoblast-osteoclast interactions. *Connect Tissue Res* 2018;59:99–107.

2. Long F. Building strong bones: molecular regulation of the osteoblast lineage. *Nat Rev Mol Cell Biol* 2011;13:27–38.

3. Mellis DJ, Itzstein C, Helfrich MH, Crockett JC. The skeleton: a multi-functional complex organ: the role of key signalling pathways in osteoclast differentiation and in bone resorption. *J Endocrinol* 2011;211:131–143.

4. Novack DV. Role of NF-κB in the skeleton. *Cell Res* 2010;21:169–182.

5. Hayden MS, Ghosh S. NF-κB, the first quarter-century: remarkable progress and outstanding questions. *Genes Dev* 2012;26:203–234.

6. Zhang Q, Lenardo MJ, Baltimore D. 30 Years of NF-κB: A Blossoming of Relevance to Human Pathobiology. *Cell* 2017;168:37–57.

7. Herrington FD, Nibbs RJB. Regulation of the Adaptive Immune Response by the IκB Family Protein Bcl-3. *Cells* 2016;5:14.

8. Yamazaki M, Fukushima H, Shin M, Katagiri T, Doi T, Takahashi T, et al. Tumor Necrosis Factor α Represses Bone Morphogenetic Protein (BMP) Signaling by Interfering with the DNA Binding of Smads through the Activation of NF-κB. *J Biol Chem* 2009;284:35987–35995.

9. Chang J, Wang Z, Tang E, Fan Z, McCauley L, Franceschi R, et al. Inhibition of osteoblastic bone formation by nuclear factor-κB. *Nat Med* 2009;15:682–689.

10. Maruyama T, Fukushima H, Nakao K, Shin M, Yasuda H, Weih F, et al. Processing of the NF-kappa B2 precursor p100 to p52 is critical for RANKL-induced osteoclast differentiation. *J Bone Miner Res* 2010;25:1058–1067.

11. Soysa NS, Alles N, Weih D, Lovas A, Mian AH, Shimokawa H, et al. The pivotal role of the alternative NF-κB pathway in maintenance of basal bone homeostasis and osteoclastogenesis. *J Bone Miner Res* 2010;25:809–818.

12. Xiao M, Inal CE, Parekh VI, Li XH, Whitnall MH. Role of NF-κB in hematopoietic niche function of osteoblasts after radiation injury. *Exp Hematol* 2009;37:52–64.

13. Cho HH, Shin KK, Kim YJ, Song JS, Kim JM, Bae YC, et al. NF-κB activation stimulates osteogenic differentiation of mesenchymal stem cells derived from human adipose tissue by increasing TAZ expression. *J Cell Physiol* 2010;223:168–177.

14. Li X, Wang J, Zhan Z, Li S, Zheng Z, Wang T, et al. Inflammation Intensity–Dependent Expression of Osteoinductive Wnt Proteins Is Critical for Ectopic New Bone Formation in Ankylosing Spondylitis. *Arthritis Rheumatol* 2018;70:1056–1070.

15. Kwon OH, Lee C-K, Lee YI, Paik S-G, Lee H-J. The hematopoietic transcription factor PU.1 regulates RANK gene expression in myeloid progenitors. *Biochem Biophys Res Commun* 2005;335:437–446.

16. Xing L, Chen D, Boyce BF. Mice Deficient in NF-κB p50 and p52 or RANK Have Defective Growth Plate Formation and Post-natal Dwarfism. *Bone Res* 2013;4:336–345.

17. Schwarz EM, Krimpenfort P, Berns A, Verma IM. Immunological defects in mice with a targeted disruption in Bcl-3. *Genes Dev* 1997;11:187–197.

18. Carmody RJ, Ruan Q, Palmer S, Hilliard B, Chen YH. Negative regulation of toll-like receptor signaling by NF-κB p50 ubiquitination blockade. *Science* 2007;317:675–678.

19. Mi H, Huang X, Muruganujan A, Tang H, Mills C, Kang D, et al. PANTHER version 11: expanded annotation data from Gene Ontology and Reactome pathways, and data analysis tool enhancements. *Nucleic Acids Res* 2017;45:D183–D189.

20. Heinz S, Benner C, Spann N, Bertolino E, Lin YC, Laslo P, et al. Simple combinations of lineage-determining transcription factors prime cis-regulatory elements required for macrophage and B cell identities. *Mol Cell* 2010;38:576–589.

21. Szklarczyk D, Gable AL, Lyon D, Junge A, Wyder S, Huerta-Cepas J, et al. STRING v11: protein–protein association networks with increased coverage, supporting functional discovery in genome-wide experimental datasets. *Nucleic Acids Res* 2018;47:D607–D613.

22. Jonason JH, O'Keefe RJ. Isolation and Culture of Neonatal Mouse Calvarial Osteoblasts. In: *Skeletal Development and Repair*.Vol 1130. Methods in Molecular Biology. Totowa, NJ: Humana Press, Totowa, NJ; 2014:295–305.

23. van 't Hof RJ, Rose L, Bassonga E, Daroszewska A. Open source software for semi-automated histomorphometry of bone resorption and formation parameters. *Bone* 2017;99:69–79.

24. Huesa C, Ortiz AC, Dunning L, McGavin L, Bennett L, McIntosh K, et al. Proteinase-activated receptor 2 modulates OA-related pain, cartilage and bone pathology. *Ann Rheum Dis* 2016;75:1989–1997.

25. Orimo H. The mechanism of mineralization and the role of alkaline phosphatase in health and disease. *J Nippon Med Sch* 2010;77:4–12.

26. Collins PE, Grassia G, Colleran A, Kiely PA, Ialenti A, Maffia P, et al. Mapping the Interaction of B Cell Leukemia 3 (BCL-3) and Nuclear Factor κB (NF-κB) p50 Identifies a BCL-3-mimetic Anti-inflammatory Peptide. *J Biol Chem* 2015;290:15687–15696.

27. Glatt V, Canalis E, Stadmeyer L, Bouxsein ML. Age-related changes in trabecular architecture differ in female and male C57BL/6J mice. *J Bone Miner Res* 2007;22:1197–1207.

28. Chen C-Y, Lee DS, Yan Y-T, Shen C-N, Hwang S-M, Lee ST, et al. Bcl3 Bridges LIF-STAT3 to Oct4 Signaling in the Maintenance of Naïve Pluripotency. *Stem Cells* 2015;33:3468–3480.

29. Wang K, Li S, Gao Y, Feng X, Liu W, Luo R, et al. BCL3 regulates RANKL-induced osteoclastogenesis by interacting with TRAF6 in bone marrow-derived macrophages. *Bone* 2018;114:257–267.

30. Legge DN, Shephard AP, Collard TJ, Greenhough A, Chambers AC, Clarkson RW, et al. BCL-3 promotes a cancer stem cell phenotype by enhancing β-catenin signalling in colorectal tumour cells. *Dis Model Mech* 2019;12.

31. Sun Y, Campisi J, Higano C, Beer TM, Porter P, Coleman I, et al. Treatment-induced damage to the tumor microenvironment promotes prostate cancer therapy resistance through WNT16B. *Nat Med* 2012;18:1359–1368.

32. Alam I, Alkhouli M, Gerard-O'Riley RL, Wright WB, Acton D, Gray AK, et al. Osteoblast-Specific Overexpression of Human WNT16 Increases Both Cortical and Trabecular Bone Mass and Structure in Mice. *Endocrinology* 2016;157:722–736.

33. Sebastian A, Hum NR, Morfin C, Murugesh DK, Loots GG. Global gene expression analysis identifies Mef2c as a potential player in Wnt16-mediated transcriptional regulation. *Gene* 2018;675:312–321.

34. Kemp JP, Morris JA, Medina-Gomez C, Forgetta V, Warrington NM, Youlten SE, et al. Identification of 153 new loci associated with heel bone mineral density and functional involvement of GPC6 in osteoporosis. *Nat Genet* 2017;1:457.

35. Nalesso G, Thomas BL, Sherwood JC, Yu J, Addimanda O, Eldridge SE, et al. WNT16 antagonises excessive canonical WNT activation and protects cartilage in osteoarthritis. *Ann Rheum Dis* 2017;76:218–226.

36. Tong W, Zeng Y, Chow DHK, Yeung W, Xu J, Deng Y, et al. Wnt16 attenuates osteoarthritis progression through a PCP/JNK-mTORC1-PTHrP cascade. *Ann Rheum Dis* 2019;78:551–561.

37. Antonczyk A, Krist B, Sajek M, Michalska A, Piaszyk-Borychowska A, Plens-Galaska M, et al. Direct Inhibition of IRF-Dependent Transcriptional Regulatory Mechanisms Associated With Disease. *Front Immunol* 2019;10:3397–23.

38. Farooq S, Leussink S, Sparrow LM, Marchini M, Britz HM, Manske SL, et al. Cortical and trabecular morphology is altered in the limb bones of mice artificially selected for faster skeletal growth. *Sci Rep* 2017;7:10527.

39. Yang L, Tsang KY, Tang HC, Chan D, Cheah KSE. Hypertrophic chondrocytes can become osteoblasts and osteocytes in endochondral bone formation. *Proc Natl Acad Sci USA* 2014;111:12097–12102.

40. Zhou X, Mark von der K, Henry S, Norton W, Adams H, de Crombrugghe B. Chondrocytes transdifferentiate into osteoblasts in endochondral bone during development, postnatal growth and fracture healing in mice. Warman ML, ed. *PLOS Genet* 2014;10:e1004820.

41. Mizuhashi K, Ono W, Matsushita Y, Sakagami N, Takahashi A, Saunders TL, et al. Resting zone of the growth plate houses a unique class of skeletal stem cells. *Nature* 2018;563:254–258.

42. Wu S, Flint JK, Rezvani G, De Luca F. Nuclear factor-κB p65 facilitates longitudinal bone growth by inducing growth plate chondrocyte proliferation and differentiation and by preventing apoptosis. *J Biol Chem* 2007;282:33698–33706.

43. Caron MMJ, Emans PJ, Surtel DAM, Cremers A, Voncken JW, Welting TJM, et al. Activation of NF-κB/p65 Facilitates Early Chondrogenic Differentiation during Endochondral Ossification. Beier F, ed. *PLoS ONE* 2012;7:e33467.

44. Wang F, Guo J, Wang Y, Hu Y, Zhang H, Chen J et al. Loss of Bcl-3 delays bone fracture healing through activating NF-κB signaling in mesenchymal stem cells. J Orthop Translat 2022;35:72-80.

Figures:

Figure 1. Whole skeletal and long bone assessment of WT and *Bcl3*$^{-/-}$ neonatal (P0) mice using micro-CT and whole-mount stains. **a,** Representative images of neonatal 3D projection models of bone mineral density. Colouration depicts high intensity voxels as red and low intensity voxels as violet. Images not to scale. **b,** Whole skeletal bone mineral density (BMD). n = 6 (WT) and 14 (*Bcl3*$^{-/-}$). **c,** Longitudinal length measurements comparing major WT and *Bcl3*$^{-/-}$ appendicular long bones of neonates, using micro-CT. n = 6-14. **d,** Tibiae and fibulae of the right legs of individual whole-mount Alizarin Red S and Alcian Blue stained mice viewed medially in brightfield. Scale bar represents 1mm. Student's *t*-test. **e,** Red/green mean pixel intensity ratio of tibial diaphysis staining, with red denoting Ca^{2+} mineral and green denoting background. **f,** Histological dual-stain (Safranin O and Fast Green) of femurs from 4-week WT and *Bcl3*$^{-/-}$ male mice. Representative images shown. Image diameter = 500μm, and inset horizontal bar = 50μm. n = 7-8. Student's *t*-test (**b** and **e**) or Mann-Whitney test (**c** and **f**). * $P < 0.05$, ** $P < 0.01$, *** $P < 0.001$ and **** $P < 0.0001$.

Figure 2. RNA-seq transcriptomic profiling of WT and *Bcl3*$^{-/-}$ osteoblasts at day 1 and day 3 following osteogenic induction. **a,** Schematic representation of experimental procedure. Following confluence, neonatal calvarial osteoblasts were treated with 50μg/ml L-ascorbic acid (AA) and 2mM β-glycerophosphate (BGP) to induce osteogenesis. **b,** Principal component analysis (PCA) of all replicates along principal components 1 and 2. **c,** Heatmap of all replicates illustrating genes significantly different in WT and *Bcl3*$^{-/-}$ cells. $P_{adj} < 0.05$, n = 3. **d,** Mean expression per gene Z-scores of 'ossification' and 'Wnt-protein binding' / Wnt gene-sets identified via gene ontology analysis of upregulated genes, in *Bcl3*$^{-/-}$ cells at day 1. Error bars denote standard deviation. **e,** Expression of select osteoblast genes at day 1 determined via quantitative PCR. Alkaline phosphatase, tissue-nonspecific isozyme (*Alpl*), collagen, type I, a-1 (*Col1a1*), osteocalcin (*Ocn*), receptor activator of nuclear factor κ B ligand (*Rankl*) osteoprotegerin (*Opg*), Runt-related transcription factor 2 (*Runx2*), osterix (*Osx*) and *Wnt16*. n = 5-6. DESeq2 outputs (**b**-**c**) and Fisher's least significant difference test (**e**). * $P < 0.05$, ** $P < 0.01$ and 'n.s.' - not significant.

Figure 3. Characterisation of WT and *Bcl3*$^{-/-}$ osteoblast function following osteogenic induction and rescue/overexpression via BCL3 mimetic peptide. Osteogenesis was induced with 50μg/ml L-ascorbic acid (AA) and 2mM β-glycerophosphate (BGP). **a**-**c,** Osteoblast production of alkaline phosphatase (ALP; **a**), collagen (**b**) and calcium mineral micro-nodules (**c**) at day 1. Complete-well representative images of group medians (top; diameter = 22mm) and the indicated magnified region (below; diameter = 182μm), accompanied by pixel quantification. Enhanced sharpness and contrast in representative images (**c**). n = 5 (WT) and 6 (*Bcl3*$^{-/-}$). **d,** Calcium mineral nodule production until day 21, with mean values superimposed per 3-day interval. Curve fitted to exponential equation using least squares fit and means shown. n = 40. **e,** Alkaline phosphatase (ALP) expression in WT and *Bcl3*$^{-/-}$ neonate calvarial osteoblasts, under osteogenic differentiation until day 3 and treated with 30mM of either control peptide (mBDP2) or BCL3 mimetic peptide (BDP2). Complete-well representative images of group medians (top; diameter = 15.6mm) and the indicated magnified region (below; diameter = 182μm), accompanied by pixel area quantification. n = 4-7. Mann-Whitney test (**a**-**c**), extra sum-of-squares F test (**d**) and paired *t*-test (**e**). * $P < 0.05$, ** $P < 0.01$, and *** $P < 0.001$.

Figure 4. Characterisation of osteoclastogenic differentiation and function of WT and *Bcl3*$^{-/-}$ cells. **a,** Bone marrow-derived non-adherent cells were stimulated with 30ng/ml M-CSF overnight and supplemented with 50ng/ml M-CSF and RANKL until days 6 or 7. **b,** Tartrate-resistant acid phosphatase (TRAP)-stained mature osteoclasts (≥3 nuclei) at day 6. Osteoclast number (N.Oc) and total osteoclast area (ΣOc.Ar). n = 3. **c,** Resorption activity of osteoclasts cultured on mineral substrate until day 7. Lighter areas indicate resorbed mineral. n = 3. **d,** Resorption activity of *Bcl3*$^{-/-}$ osteoclasts, under osteoclastogenic differentiation until day 7, treated with 30μM control peptide (mBDP2) or BCL3 mimetic peptide (BDP2). n = 5. **e,** WT or *Bcl3*$^{-/-}$ (from a *Bcl3*$^{-/-}$*::p53*$^{fl/-}$ strain*)* osteoblasts were co-cultured with WT CD14^{+} monocytes in osteogenic medium up to 9 days. **f,** TRAP-stained osteoclast number and area at day 9. n = 3. **g,** Supernatant levels of receptor activator of NF-κB ligand (RANKL), osteoprotegerin (OPG). n = 5-6. Representative complete-well (above; diameter = 6.4mm) and magnified (below; diameter = 182μm) images of medians (b-f). Student's *t*-test (**b**-**c, f**) and paired *t*-test (**d**). Two-way ANOVA with Fisher's LSD multiple comparison (**g**). * $P < 0.05$, ** $P < 0.01$, *** $P < 0.001$ and **** $P < 0.0001$.

Figure 5. Phenotypic analyses of 20-week WT and *Bcl3*$^{-/-}$ male mice. **a,** Representative volumetric bone density visualisations of the distal femoral trabecular region (images not to scale). Key three-dimensional morphometric parameters: percent bone volume density (BV/TV), trabecular number (Tb.N), and trabecular thickness (Tb.Th). **b,** Biomechanical three-point break test of the tibial mid-shaft. Force-displacement curve, fitted to cubic equation using least squares fit. Derivative parameters, include ultimate load (maximum), stiffness (linear slope) and work to failure (curve area). n = 29 (*Bcl3*$^{-/-}$) and 31 (WT). **c,** Dynamic histomorphometry of the combined trabecular and endocortical regions of the proximal metaphysis of tibiae. Representative images of sections showing fluorescent calcein double-label (light blue), bone matrix (dark blue) and bone marrow (green). Mineral apposition rate (MAR). Image diameter = 190. n = 3. **d,** Serum bone turnover markers, procollagen type 1 amino-terminal peptide (P1NP), carboxyl-terminal crosslinks peptide of type 1 collagen (CTX1), osteoprotegerin (OPG) and receptor activator of nuclear factor κ B ligand (RANKL). n = 10. Welch's *t*-test or Mann-Whitney test used for pairwise comparisons throughout and extra sum-of-squares F test (**b**). * $P < 0.05$, ** $P < 0.01$, *** $P < 0.001$, **** $P < 0.0001$ and 'n.s.' - not significant.

Figure 6. Osteoarthritic disease model of the destabilised medial meniscus (DMM) in WT and *Bcl3*$^{-/-}$ mice. **a,** Knee joint (left) and cross-section of the tibial subchondral bone plateau (right), illustrating the protrusion of pathologic osteophytes (arrowheads), 14 days post-surgery. Representative images shown in bone density spectrum. Anterior (*a*), posterior (*p*), lateral (*l*), medial (*m*). **b,** Total bone volume (BV) of osteophytes in WT and *Bcl3*$^{-/-}$ mice subjected to DMM procedure. **c,** OARSI histopathology scoring of the medial tibial plateau (MTP) of WT and *Bcl3*$^{-/-}$ mice, 14 days post-surgery. **d,** Dual-stained sections of identical WT and *Bcl3*$^{-/-}$ joint samples in **a**, showing red subchondral osteophyte (black arrowheads) and hairy articular cartilage damage (grey arrowheads). Image diameter = 1mm. **e,** Tibial subchondral bone medial/lateral bone volume ratios in contralateral (unoperated) and ipsilateral (operated) knees. Welch's *t*-test (**b** and **c**) and ratio paired *t*-test (**e**). n = 11 (*Bcl3*$^{-/-}$) and 13 (WT). * $P < 0.05$ and 'n.s.' - not significant. **f,** Schema of perturbed skeletal steady-state in mice lacking BCL3. Homeostatic progression of both osteogenesis and osteoclastogenesis is dependent upon NF-κB activity, regulated by BCL3. Herein we have shown that BCL3 absence accelerates differentiation and increases function of both osteoblasts and osteoclasts.

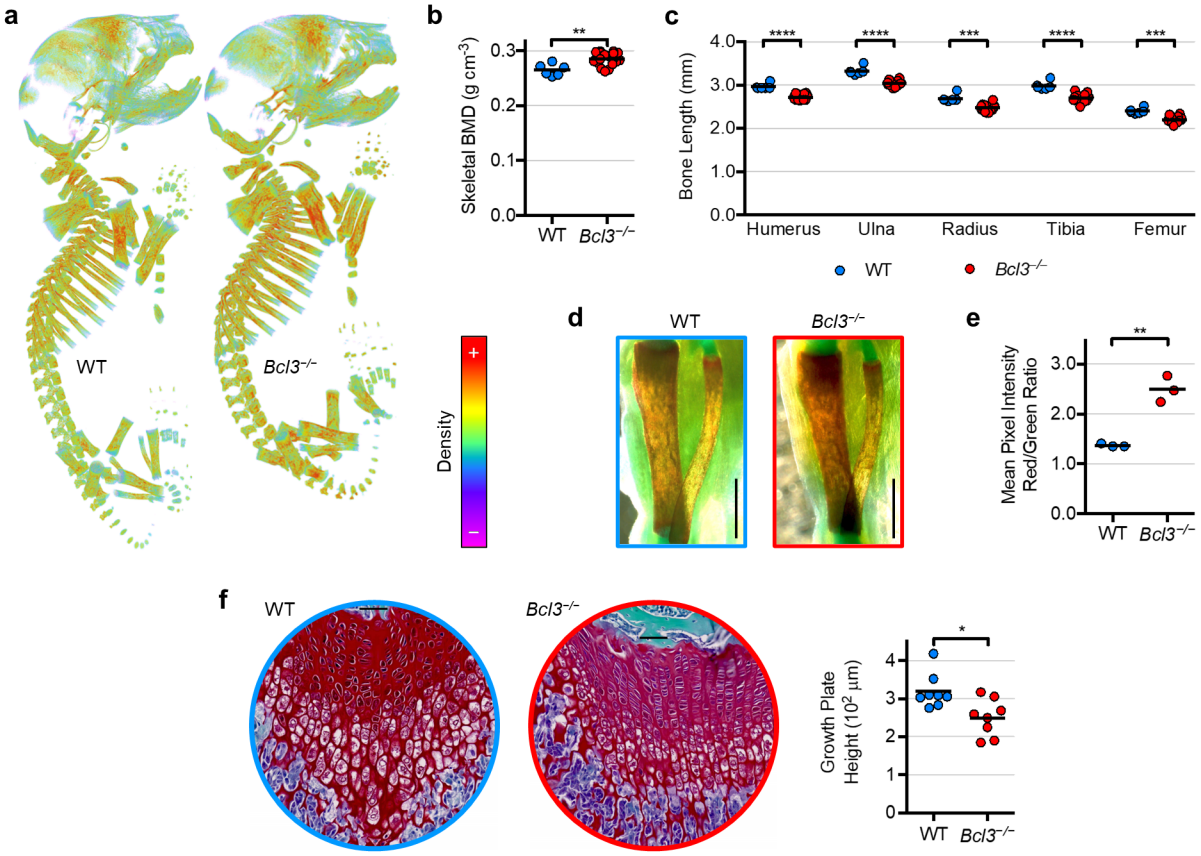

Figure 1.TIF

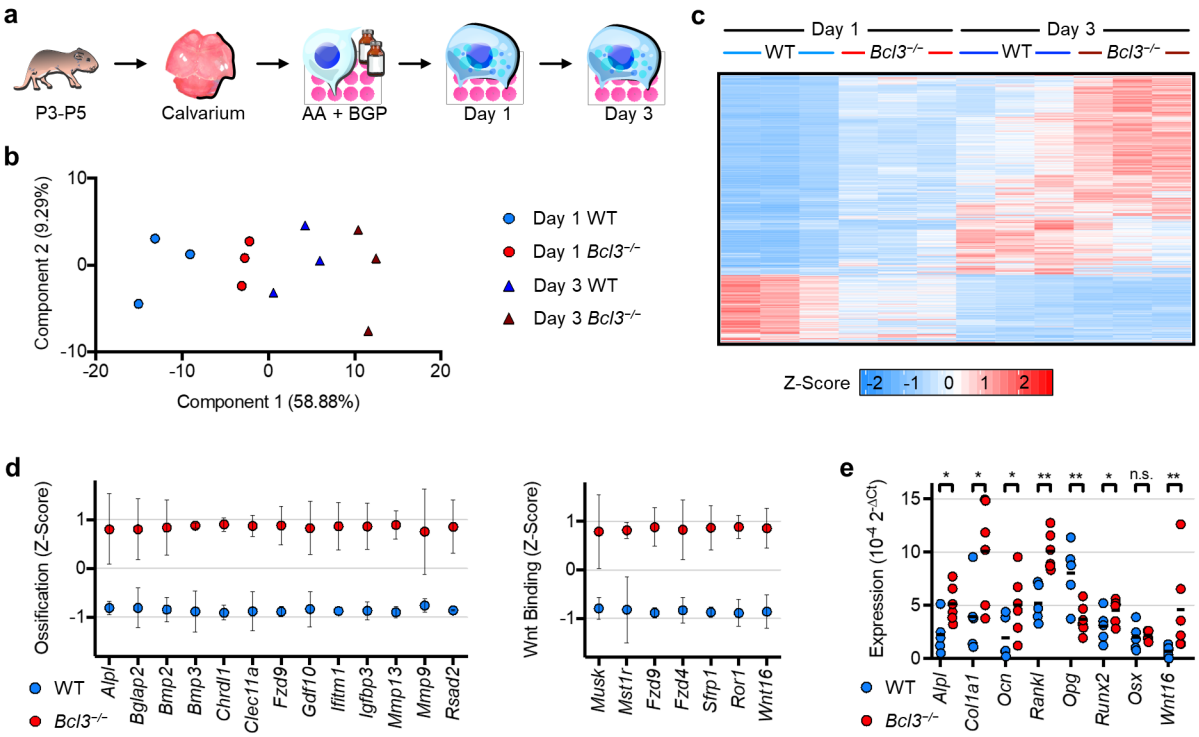

Figure 2.TIF

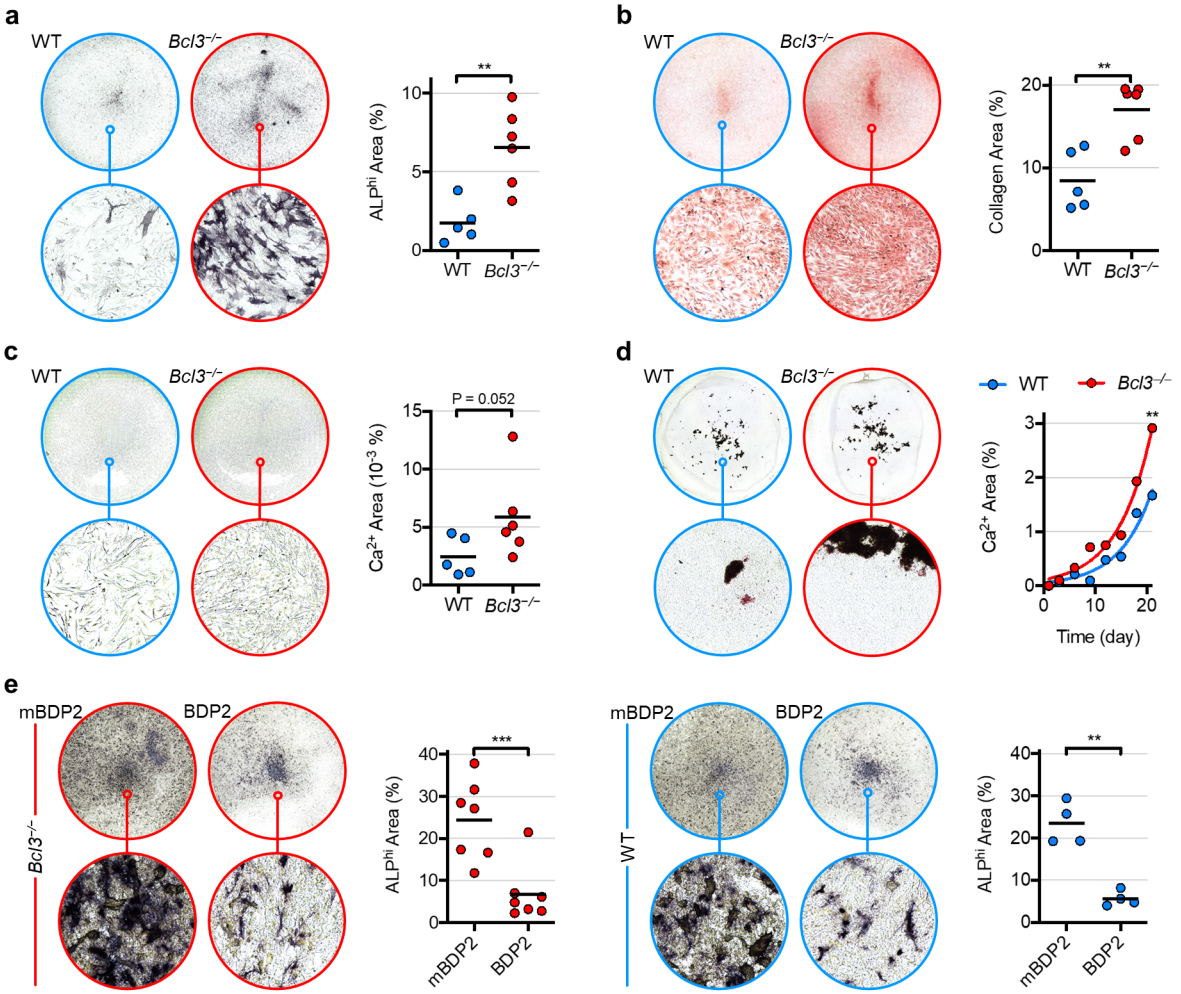

Figure 3.TIF

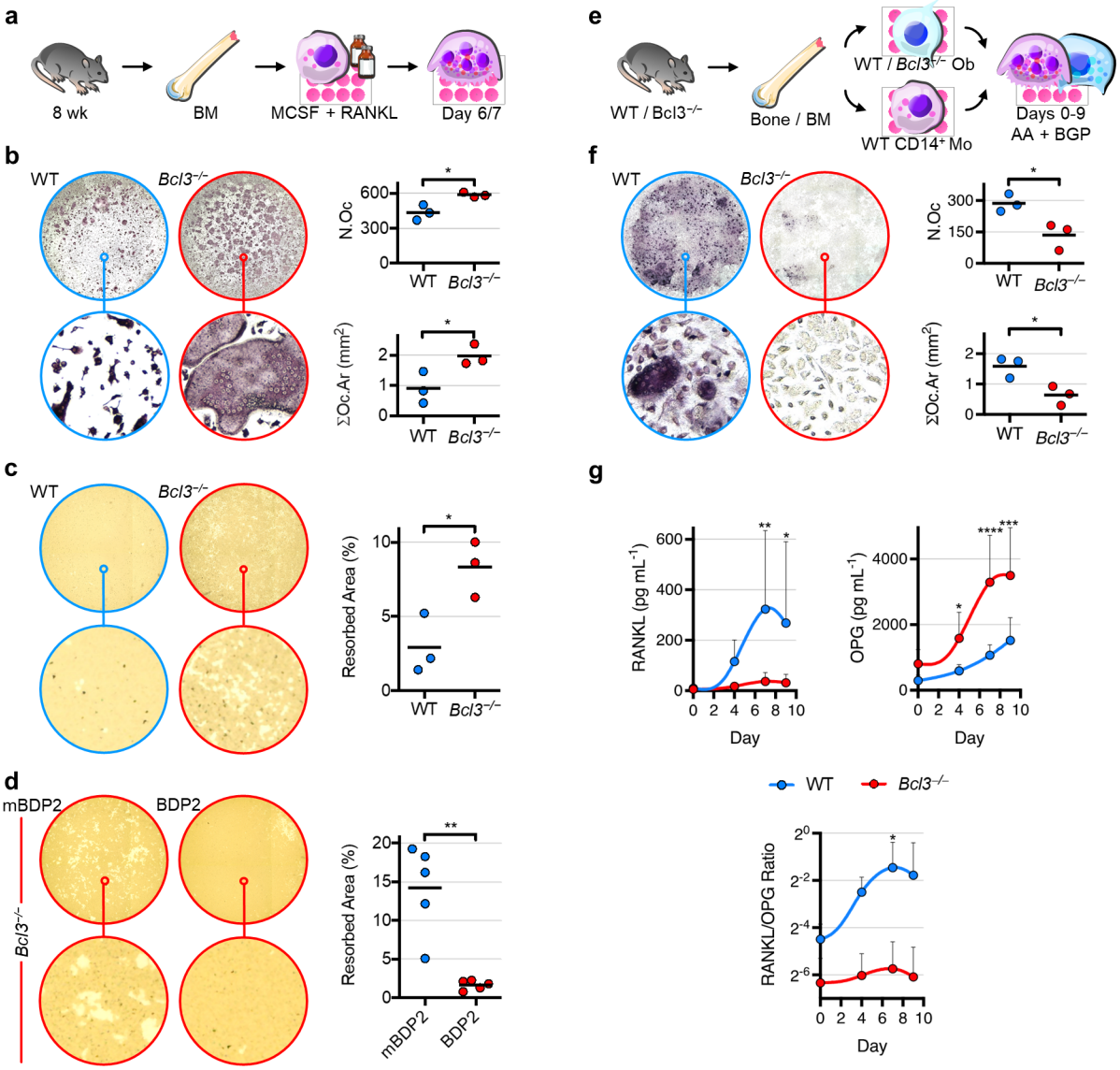

Figure 4.TIF

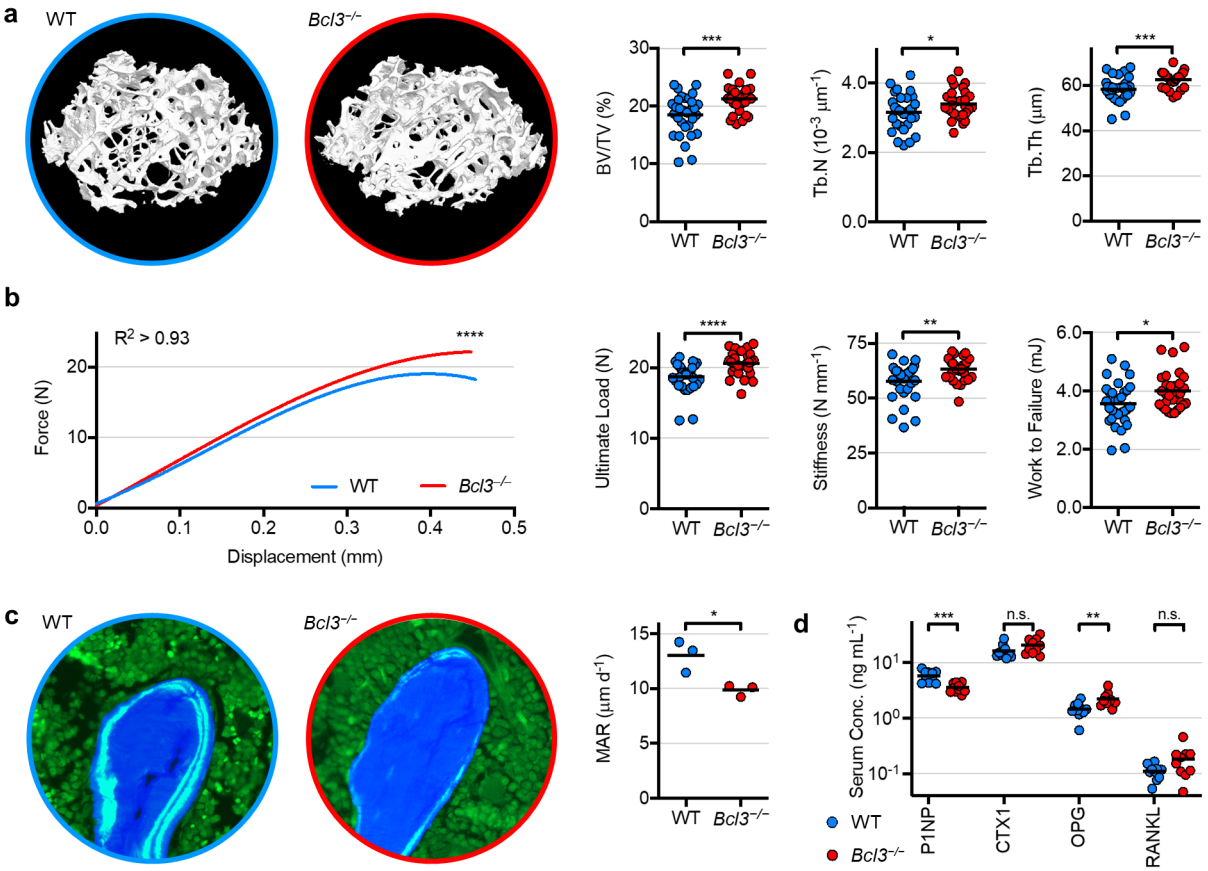

Figure 5.TIF

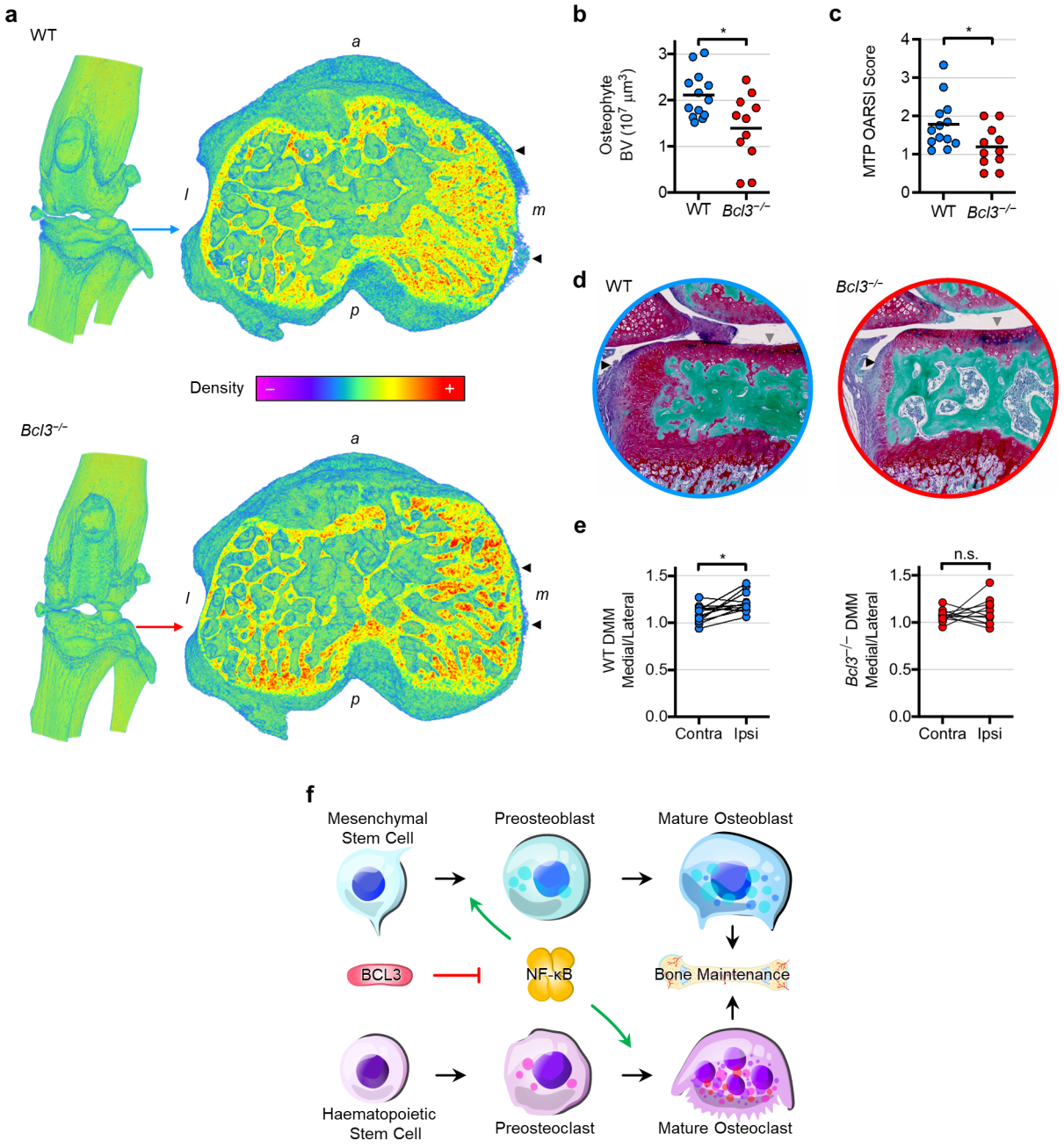

Figure 6.TIF

The IκB Protein BCL3 Controls Osteogenesis and Bone Health

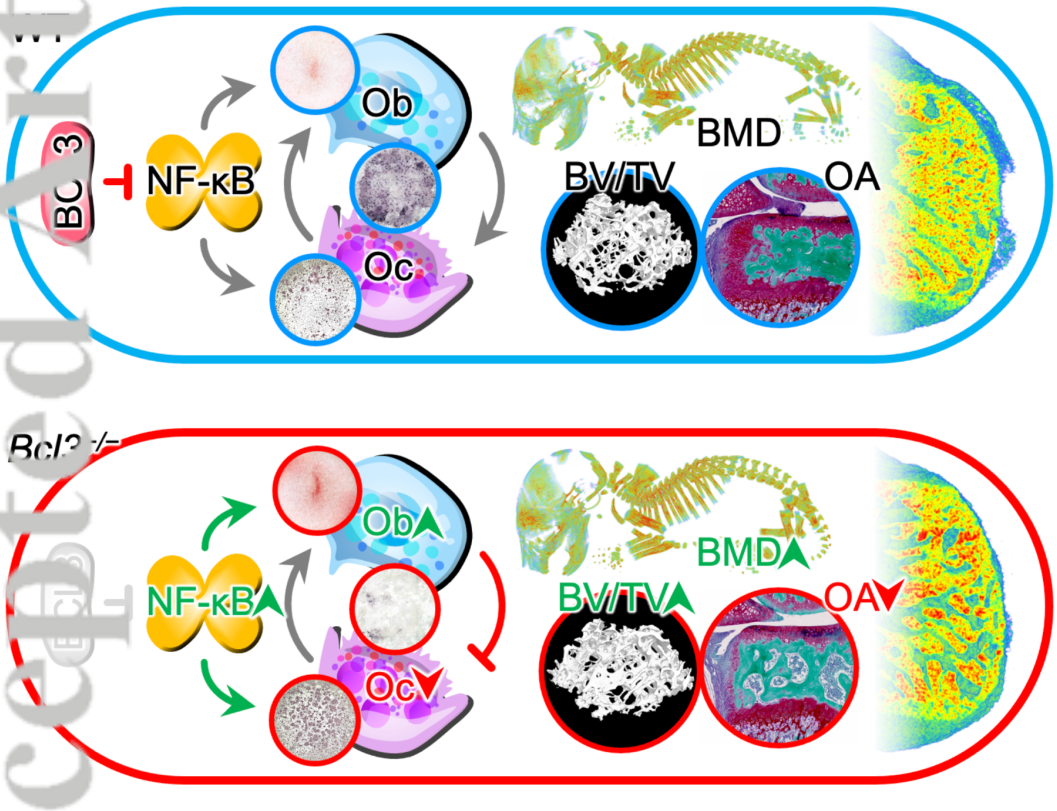

Key Results

- Knockout of Bcl-3 (*Bcl3*$^{-/-}$), regulator of NF-κB, accelerates osteogenesis & osteoclastogenesis compared to wild-type (WT)
- *Bcl3*$^{-/-}$ osteoblasts (Ob) inhibit osteoclasts (Oc) in co-culture
- *Bcl3*$^{-/-}$ increases in vivo bone mineral density (BMD) in neonates
- Adult *Bcl3*$^{-/-}$ mice maintain increased bone density (BV/TV) and strength
- Pathologic osteoarthritis (OA)-driven osteophytes reduced in *Bcl3*$^{-/-}$ mice

Jaffery H, Huesa C, Chilaka S, et al. The IκB protein BCL3 controls osteogenesis and bone health. Arthritis Rheumatol 2023.

Arthritis & Rheumatology ACR American College of Rheumatology

Jaffery graphical abstract 20-1871.png